Research Article Vol. 31, No. 5 / 27 Feb 2023 / Optics Express 9098
Optics EXPRESS

Laser ultrasonic imaging of subsurface defects with the linear sampling method

VENKATALAKSHMI V. NARUMANCHI,[1] FATEMEH POURAHMADIAN,[2] JORDAN LUM,[3] ANDREW TOWNSEND,[3] JOSEPH W. TRINGE,[3] DAVID M. STOBBE,[3] AND TODD W. MURRAY[4,*]

[1]*Department of Electrical and Computer Engineering, University of Colorado Boulder, Boulder, CO 80309, USA*
[2]*Department of Civil, Environmental, and Architectural Engineering, University of Colorado, Boulder, CO 80309, USA*
[3]*Lawrence Livermore National Laboratory, Livermore, CA 94550, USA*
[4]*Department of Mechanical Engineering, University of Colorado Boulder, Boulder, CO 80309, USA*
[*]*todd.murray@colorado.edu*

Abstract: Laser ultrasonics is a remote nondestructive evaluation technique suitable for real-time monitoring of fabrication processes in semiconductor metrology, advanced manufacturing, and other applications where non-contact, high fidelity measurements are required. Here we investigate laser ultrasonic data processing approaches to reconstruct images of subsurface side drilled holes in aluminum alloy specimens. We demonstrate through simulation that the model-based linear sampling method (LSM) can perform accurate shape reconstruction of single and multiple holes and produce images with well-defined boundaries. We experimentally confirm that LSM produces images that represent the internal geometric features of an object, some of which may be missed by conventional imaging.

1. Introduction

Laser ultrasonics is a non-contact nondestructive inspection technique that can be advantageous relative to conventional ultrasonics in harsh environments or in settings where contact to the sample is not possible or desirable [1]. The technique has seen widespread adoption in, for example, measuring the mechanical properties of thin films [2,3], monitoring materials behavior in high temperature environments [4,5], and, more recently, in the inspection and potential online monitoring of additively-manufactured parts and processes [6–8]. Laser sources and detectors can be rapidly moved over a sample surface using galvanometric scanners to generate an array of ultrasonic data. Post processing can then be employed to create subsurface images of material inhomogeneities or to map materials properties.

A thermoelastic laser source generates longitudinal, shear, and surface acoustic waves in a semi-infinite half-space. In finite samples the mode conversion of bulk waves at interfaces complicates the detected wave field. Ultimately, one seeks to maximize sample information including defect presence, size, and shape. This work integrates laser ultrasonics and analytics to facilitate high-fidelity *in situ* imaging of such anomalies in elastic solids. Specifically, we identify a suitable waveform inversion tool for laser ultrasonic experiments and demonstrate the utility of the linear sampling method (LSM) of the inverse scattering theory for imaging. We then compare results from LSM to the conventional delay and sum (DAS) approach.

Delay and sum methods (also known as time-of-flight methods) synthetically refocus the measured waveforms at various locations in the sample by calculating the travel time of probing waves along potential pathways between sources and receivers. An example of this approach is the synthetic aperture focusing technique (SAFT) [9,10] which performs time- or frequency-domain refocusing of signals between sources and receivers. Laser ultrasonic imaging using

#485084 https://doi.org/10.1364/OE.485084
Journal © 2023 Received 6 Jan 2023; revised 12 Feb 2023; accepted 17 Feb 2023; published 24 Feb 2023

Optics EXPRESS

SAFT in finite samples suffers from the fact that images are reconstructed using a particular wave mode (longitudinal or shear waves) and the expected ray path must be specified. It is known that a single-mode elastic wave impinging on a boundary generates multi-modal reflections (and/or transmissions) propagating in different directions with distinct velocities. Such mode conversion [11] along with potential interactions with multiple surfaces of different boundary conditions result in quite complex propagation patterns which may lead to ray-path-dependent images featuring various artifacts. Artifacts that occur due to this kind of cross-talk have been previously identified and suppressed to improve defect detection [12,13]. Iterative algorithms have also been applied to remove such artifacts by using prior knowledge in the form of sensitivity maps [14–16]. Nevertheless, these artifacts are unique for different sensing configurations, and an optimization process will have to be repeated for different experimental systems. It is therefore beneficial to have an imaging algorithm that uses all the recorded information independent of the sensing configuration and does not require ray tracing.

Another approach to ultrasonic imaging is time-reversal [17–19], wherein recorded wavefields are back-propagated into the sample to refocus the energy onto hidden scatterers based on the reciprocity principle. Adopting a similar approach, the linear sampling method (LSM) provides a different non-iterative waveform inversion process [20]. For a given background, LSM makes use of the scattering footprints of hidden obstacles to recover their support without requiring *a priori* knowledge of their geometric or material properties, or boundary conditions. This is accomplished by reducing the error between linear compositions of scattered measurements and the impulse response of the background at various sampling points in a search region. It has been applied in a wide range of applications including electromagnetics, acoustics and elastodynamics [21–23]. Recent laboratory demonstration of LSM for ultrasonic imaging [24,25] makes it an appealing candidate for inverting the complex waveforms obtained by laser ultrasonics experiments.

In this paper we demonstrate the feasibility of the linear sampling method with laser ultrasonic data through time domain finite element simulations validated with experiments. We start by imaging a simple sample with a single hole defect. We next image a sample with two holes horizontally offset from one another to investigate cross-talk. Finally, we image two holes vertically offset from one another, with the hole on the top being larger and shadowing the lower hole. For all samples we compare the LSM reconstructions against DAS results. This study then establishes how LSM can image hidden objects that may missed by conventional approaches.

2. Background and theory

Scattered displacement data are employed to reconstruct the sample's interior within a designated search volume using two imaging schemes: DAS and LSM. The DAS algorithm calculates the time-of-flight along specified paths between sources, potential defects, and receivers to build a map of hidden anomalies [26]. LSM, by contrast, makes use of the measurement spectra for non-iterative data inversion as described in this section. Experiments involve multimodal ultrasonic waves induced by a pulsed laser on the incident surface S^{inc} which is a subset of the specimen's boundary, while the resulting displacements are captured by a continuous wave (CW) laser on the observation surface S^{obs}. In this setting, let $u^{\text{f}}(\boldsymbol{x}, t; \boldsymbol{y})$ (*resp.* $u^{\text{t}}(\boldsymbol{x}, t; \boldsymbol{y})$) denotes the response of the intact (*resp.* damaged) specimen along the CW laser beam at $\boldsymbol{x} \in S^{\text{obs}}$ due to excitation at $\boldsymbol{y} \in S^{\text{inc}}$ as a function of time t. The scattered field $u^{\text{s}}(\boldsymbol{x}, t; \boldsymbol{y})$ is given by

$$u^{\text{s}}(\boldsymbol{x}, t; \boldsymbol{y}) = [u^{\text{t}} - u^{\text{f}}](\boldsymbol{x}, t; \boldsymbol{y}), \quad \boldsymbol{x} \in S^{\text{obs}}, \ y \in S^{\text{inc}}, \ t \in (0 \ \ T], \tag{1}$$

wherein T indicates the total measurement period. Now, let $\mathrm{F}(\boldsymbol{x}, \omega; \boldsymbol{y})$ be the spectral scattering operator such that

$$[\mathrm{F}(\mathrm{g})](\boldsymbol{x}, \omega) := \int_{S^{\text{inc}}} \hat{u}^{\text{s}}(\boldsymbol{x}, \omega; \boldsymbol{y})\, \mathrm{g}(\boldsymbol{y}, \omega)\, \mathrm{d}S_{\boldsymbol{y}}, \quad \omega \in \Omega := [\omega_{\min} \ \ \omega_{\max}], \tag{2}$$

Optics EXPRESS

wherein $\hat{u}^s$ is the Fourier-transformed scattered displacement u^s, and $g(\boldsymbol{y}, \omega)$ is the spectrum of source density on S^{inc}. The LSM indicator is then built by probing the range of the discretized scattering operator $\boldsymbol{F}$ by solving

$$\begin{aligned} &\boldsymbol{Fg} = \boldsymbol{U}, \quad F(N_m k + i, N_s k + j) = \hat{u}^s(\boldsymbol{x}_i, \omega_k; \boldsymbol{y}_j), \\ &U(N_m k + i, l) = \Phi_l(\boldsymbol{x}_i, \omega_k; (Z, \boldsymbol{n})_l), \quad g(N_s k + j, l) = g((\boldsymbol{x}_i, \omega_k; (z, \boldsymbol{n})_l)) \\ &i = 0, \cdots, N_m - 1, j = 0, \cdots, N_s - 1, k = 0, \cdots, N\omega - \ 1, l = 0, \cdots, N_{sp} - 1, \end{aligned} \tag{3}$$

for wavefront density $\boldsymbol{g}$**.** Note that in constructing $\boldsymbol{F}$, it is assumed that in the test configuration the incident and observation surfaces are respectively discretized by N_s and N_m points, while Ω is sampled Φ_l at N_ω frequencies. In parallel, a set of trial pairs $(z, \boldsymbol{n})_l, l = 0, \ldots, N_{sp} - 1$, is defined in the sampling region, i.e., a subset of the background domain where we search for anomalies, wherein z_l indicates the sampling point coordinates and $\boldsymbol{n}_l$ is a unit polarization vector. For every pair, the impulse response $\boldsymbol{\Phi}_l$ of the background to a dipole force applied at z_l with polarization $\boldsymbol{n}_l$ is computed on the observation grid $\boldsymbol{x}_i \in S^{\text{obs}}, i = 0, \ldots, N_m - 1$, at $\omega_k \in \Omega, k = 0, \ldots, N_\omega - 1$. These synthetic displacements are then used to construct the right-hand side $\boldsymbol{U}$ of the scattering equation. For every $(z, \boldsymbol{n})_l$, Eqn. (3) is solved via non-iterative minimization of the Tikhonov cost function

$$\boldsymbol{g}_{z,\boldsymbol{n}} := \underset{\boldsymbol{g}_{z,\boldsymbol{n}}}{\text{argmin}} \left(\| \boldsymbol{F}\boldsymbol{g}_{z,\boldsymbol{n}} - \Phi_l \|^2 + \eta_l \| \boldsymbol{g}_{z,\boldsymbol{n}} \|^2 \right), \tag{4}$$

where η_l is a regularization parameter calculated via the Morozov discrepancy principle [27]. Whereby, the LSM indicator L, affiliated with the bandwidth Ω, is defined in the sampling region as the following

$$L(z; \Omega) : \frac{1}{\|\boldsymbol{g}_z\|}, \quad \boldsymbol{g}_z := \underset{\boldsymbol{g}_{z,\boldsymbol{n}}}{\text{argmin}} \| \boldsymbol{g}_{z,\boldsymbol{n}} \| . \tag{5}$$

In this setting, the main LSM theorem [21] requires that L achieves its highest values at the loci of hidden scatterers, while assuming near-zero values otherwise. The selection of the regularization parameter requires an estimate of the noise level in the scattered field. In this study, the reconstructions are conducted for a set of noise level estimates in order to identify the appropriate value. Once this parameter is identified, the reconstructions remain remarkably stable with not much sensitivity to perturbations in signal processing or other inversion parameters.

3. Numerical simulations and results

We simulated the laser ultrasonic response with the commercial time domain finite element software (OnScale). We model our test geometry as a 2D problem under the assumption of plane strain, with an infinite laser line source used to generate the ultrasonic signals. The spatial profile of the line source is given by a Gaussian of full-width-at-half-max (FWHM) of 50 µm. The initial surface force imparted into the sample is proportional to the generated thermal gradient, and thus proportional to the derivative of the laser source in space. Nanosecond surface heating occurs quickly with respect to the cooling process. To model the temporal profile produced by a 9.0 ns heating pulse, we assume the temporal forcing function is the integral of the heating pulse. The simulation output is then the normal surface displacement in response to this laser heating.

We performed numerical simulations on aluminum plates with a density of 2.73 g/cm^3, shear wave velocity (c_T) of 3224 m/s, and longitudinal wave velocity (c_L) of 6482 m/s. The thickness of the plates was approximately 3.0 mm, and traction-free boundary conditions were employed on the top and bottom surfaces. Absorbing boundary conditions were used on the sides to prevent reflections. Figure 1(a) shows the measurement array on the surface of the sample, with a total aperture of 9 mm and a spacing between measurement points of 75 µm. This spacing corresponds to approximately one-half wavelength of the shear wave at 20 MHz. Within the aperture there

Optics EXPRESS

are 121 total source and receiver positions. This sensing configuration was chosen so that there is a dense enough dataset to perform the synthetic wave-front shaping via the LSM inversion. Images of scatterers are reconstructed within a 2.1 mm × 2.1 mm window centered between the plate walls and directly below the array.

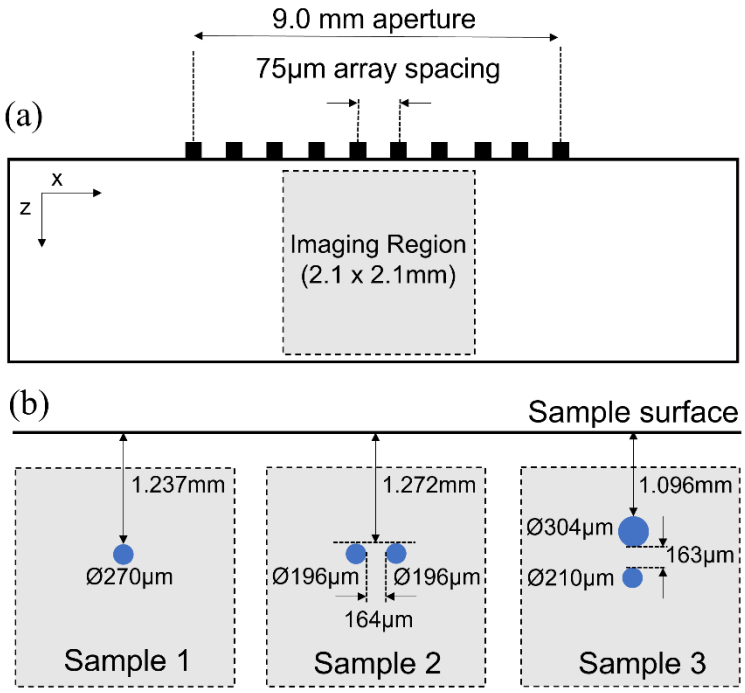

Fig. 1. Schematic of the 2D simulation setup. (a) A 121-element array is created in the middle of the sample to record data. The total aperture length is 9 mm with an array spacing of 75 μm. (b) The three samples to be imaged are shown within the imaging region.

To perform the LSM inversion, a library $\mathbf{U}$ (see Eqn. (3)) is required. Within the imaging region shown in Fig. 1(a), we chose a rectangular grid consisting of 71×71 points as centers to calculate impulse responses. These points are spaced by 30 μm. At one point within this grid, a dipole impulse force is applied to the sample to generate a wave field, and the resulting out- of-plane time domain response is determined at each of the 121 detection positions. This process is repeated for all points on the grid. All time domain waveforms are then multiplied by a Tukey window of cosine factor 0.1 and Fourier transformed. Once in the frequency domain, the amplitudes of the individual frequencies within the bandwidth Ω are used to build the library $\mathbf{U}$. The DAS images are also computed in the same reconstruction region using the time domain signals filtered within the same bandwidth.

We simulated experimental data using sample 1 shown in Fig. 1(b). The sample has a 270 μm diameter hole, and the top of the hole is 1.237 mm below the sample surface. The source is placed on the first array element on the surface, and the out of plane displacement response is collected at all 121 detection points. The process is then repeated for every source position thus generating a full matrix of ultrasound data. An analogous set of simulations is performed on a pristine sample of the same dimensions but without a hole to generate a full "background data" matrix. Figure 2(a) shows the out-of-plane displacement as a function of time for a single source to detector distance (1.95 mm) for sample 1 and the background data. For sample 1, the source is located approximately 1.0 mm to the left of the hole, and the receiver is on the right side. The waveforms are bandpass filtered between 6 MHz and 21 MHz using a 2nd order

Optics EXPRESS

Butterworth filter. In the background waveform, the first signal in time is the surface skimming longitudinal wave (SSL), followed by the surface acoustic wave (SAW), and several direct and mode-converted longitudinal and shear bulk waves (BW) reflected from the back surface. In the sample 1 waveform, additional arrivals are observed associated with scattering from the hole including a direct shear wave reflection (SS) and a half-skip shear wave which interacts with both the hole and the back surface of the sample (SSS).

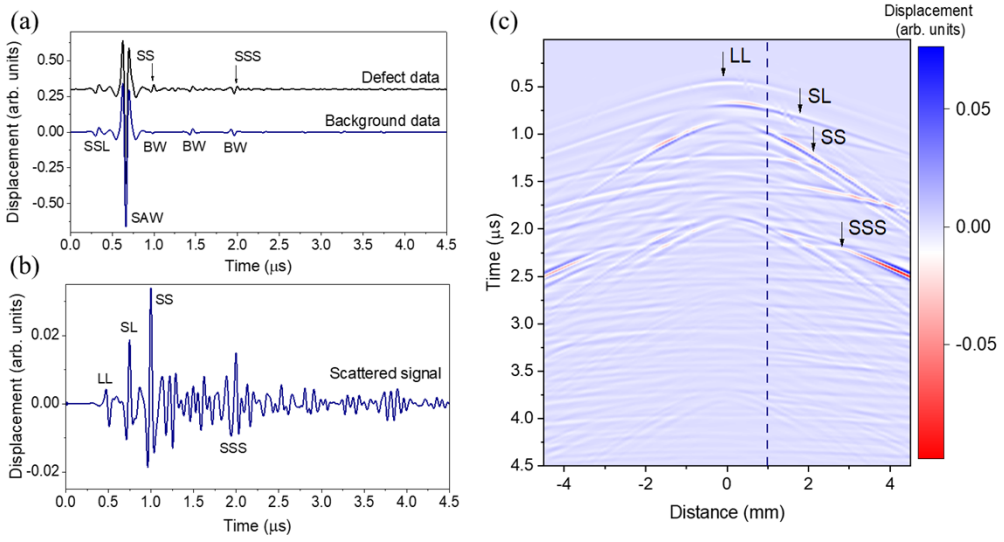

Fig. 2. (a) A simulated waveform from sample 1 and the corresponding background signal when the source and receiver distance is 1.95 mm with the hole located approximately halfway in between them. (b) The subtracted waveform showing the scattering signature from the hole. (c) The scattered field at all the detector positions in the array. The dashed line is the location of the waveform in (b).

To isolate the impact of the hole from the background wave field, the two signals are subtracted and the "scattered field" result is shown in Fig. 2(b). Here two additional arrivals that had been hidden by the SAW can be identified: a direct longitudinal reflection (LL) from the hole and an arrival associated with a shear wave that travels from the source to the hole where it is mode converted to a longitudinal wave that propagates to the detector (SL). In addition, a complex set of arrivals is seen that is associated with multiple reflections within the sample that have interacted with the hole. Figure 2(c) shows the scattered field from all of the detectors in response to a source located 1.0 mm to the left of the hole, and the dashed line shows the location that the signals in Fig. 2(a) were recorded. The color scale represents the normal displacement amplitude, with the amplitude normalized to the SAW amplitude in the data set prior to subtraction. The prominent arrivals labeled for the single trace in Fig. 2(b) are labeled on the image. The scattered signals arriving later in time provide additional information regarding the hole size and location. The amplitude for each arrival changes with detector position due to both the longitudinal and shear wave directivity of the thermoelastic laser source and the angle-dependent mode conversion at the hole and back surface.

The DAS reconstruction in the time domain and the LSM imaging technique in the frequency domain are performed on the scattered field to image subsurface inhomogeneities. To perform the LSM inversion, the scattered field signals are multiplied by a Tukey window of cosine factor 0.05 and Fourier transformed. The amplitudes (corresponding to Ω) from 6 MHz – 21 MHz are collected in steps of 0.3 MHz and used to construct the $\mathbf{F}$ matrix. The images reconstructed using

Optics EXPRESS

the direct longitudinal and shear wave arrivals using DAS are shown in Fig. 3(a) and Fig. 3(b), respectively. The hole is present in both images, but there is little indication of the shape or extent of the hole. The image shown in Fig. 3(c) was reconstructed using the LSM algorithm, and in contrast, shows the distinct edges of the circular hole. Figure 3(d) shows the amplitude of a horizontal line cut through the center of the circular inclusion, together with the actual extent of the inclusion at that point (dashed line). While quantification of the accuracy of the imaging technique in sizing defects is difficult, it is apparent that the LSM is advantageous in reconstruction. This is because the LSM algorithm takes into account the entire wave field rather than a single wave mode.

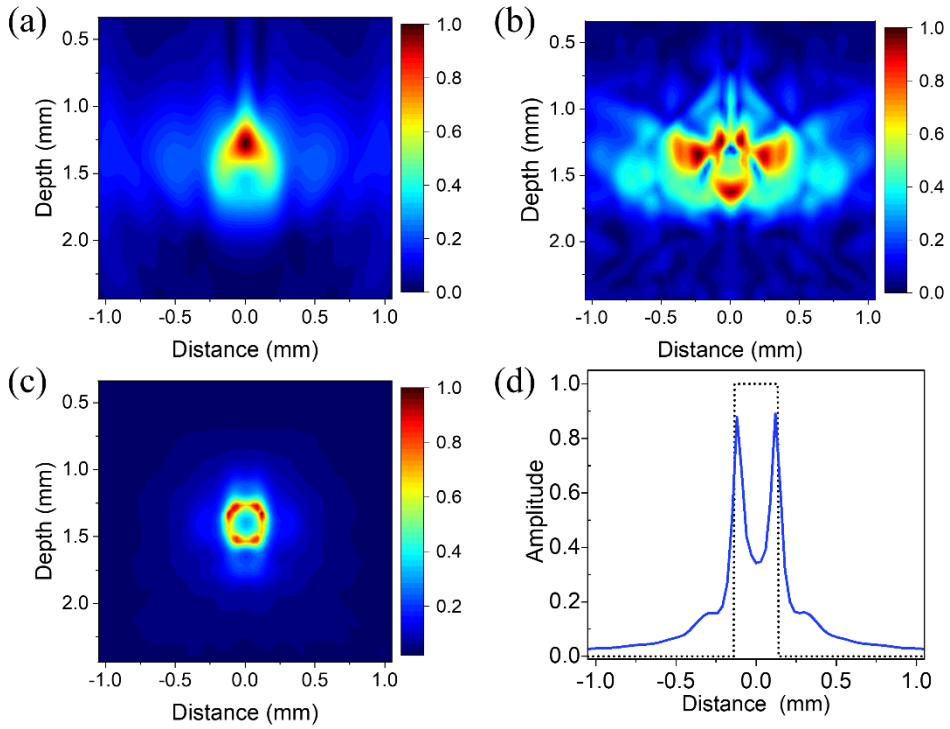

Fig. 3. DAS reconstruction of the direct (a) longitudinal and (b) shear arrivals within the 6 MHz-21 MHz bandwidth. (c) LSM reconstruction of the defect in the same frequency range discretized in 0.3 MHz steps. (d) A line profile of the LSM reconstruction taken at a depth of z = 1.36 mm overlaid with the true object dimensions at the same depth (dashed line).

We investigated the effect of random noise by adding white noise to the sample data set, assuming that we have a background data set that has very low noise with respect to the collected data. Such a data set could be measured or obtained through numerical simulation. The noise level is arbitrarily defined as the standard deviation of the added noise as a percentage of the mean SAW amplitude, where both have been filtered within the reconstruction bandwidth Ω. Note that the SAW amplitude is high compared to the amplitude of the reflections from the hole, and that the noise estimates in this scenario are consistent with those observed experimentally. Three levels of noise are added: 0.1%, 0.5%, and 3%. Figure 4(a) shows waveforms with noise added for a source-to-receiver distance of 1.95 mm and filtered over the reconstruction bandwidth Ω. At a 3% noise level, for example, it is difficult to identify any arrivals from the hole or back wall. The LSM reconstructions are shown in Fig. 4(b)-(d) for 0.1%, 0.5%, and 3% noise levels,

Optics EXPRESS

respectively. At 0.1% noise, the reconstruction is similar to the noise-free case shown in Fig. 3(c). When the noise is increased to 0.5%, the hole is still visible, but the background level increases from close to 0 to approximately 0.2. At 3% noise, the LSM technique starts to break down, resulting in artifacts and blurring of the edges of the hole. We note that DAS is more robust to noise than LSM. At a 3% noise level, for example, we observe little change in the DAS image compared to the noise free case.

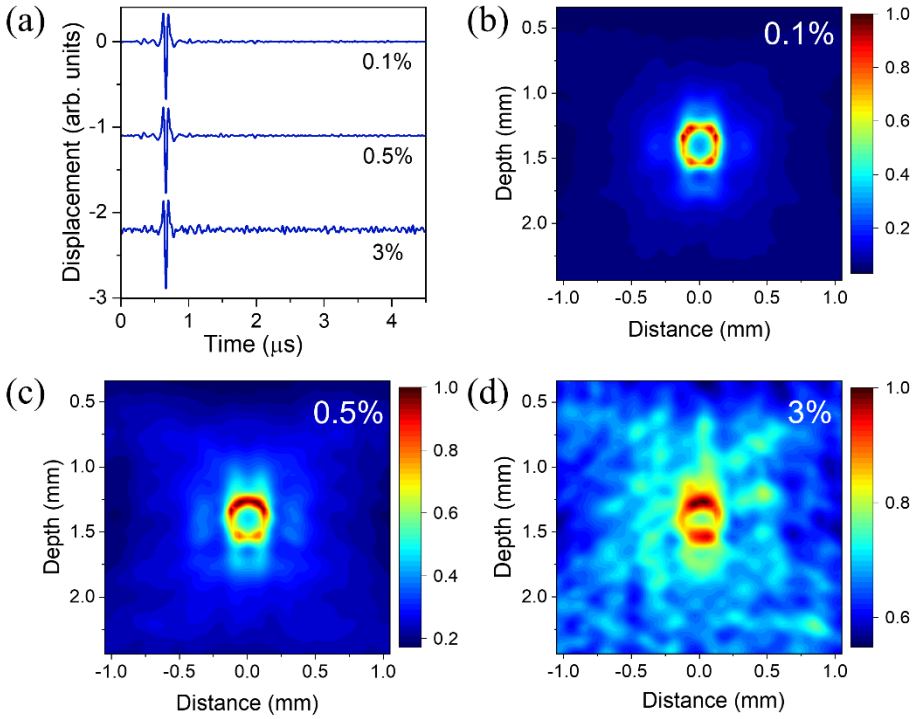

Fig. 4. LSM reconstruction of sample 1 in the presence of noise. (a) Waveforms when the source-to-receiver distance is 1.95 mm with noise added. LSM reconstructions with noise added of (b) 0.1%, (c) 0.5%, and (d) 3%.

We next describe results obtained on the more complex objects. Sample 2 (see Fig. 1(b)) has two holes of diameter 196 μm separated by 163 μm edge-to-edge. The LSM inversion of this object is shown in Fig. 5(a) and the DAS reconstruction using the direct longitudinal arrivals is shown in Fig. 5(b). Both approaches can identify the presence of the holes. However, the DAS reconstruction is dominated by the direct reflection from the top of the hole and reconstruction of the hole shape is not possible. The LSM inversion captures both the location and shape of the holes. We note that other ray paths can also be used in DAS to obtain additional information. Half-skip paths (longitudinal, shear, or mode converted), for example, may be more sensitive to the location of the bottom surface of the hole. Nevertheless, LSM has the advantage that it automatically takes into account all ray paths, combining multiple views to create a single reconstructed image.

Sample 3 (see Fig. 1(b)) has two holes that are vertically separated by 164 μm edge-to-edge. The hole on the top has a diameter of 304 μm which shadows a smaller 210 μm hole below it. The image of this object using LSM inversion is shown in Fig. 5(c). Both holes are present, but the edges between the holes are poorly reconstructed because few ray paths interact with these surfaces. In addition, multiple scattering events between the holes could lead to artifacts as these are not included in the scattering library **U**. Figure 5(d) gives the DAS image using the direct

Optics EXPRESS

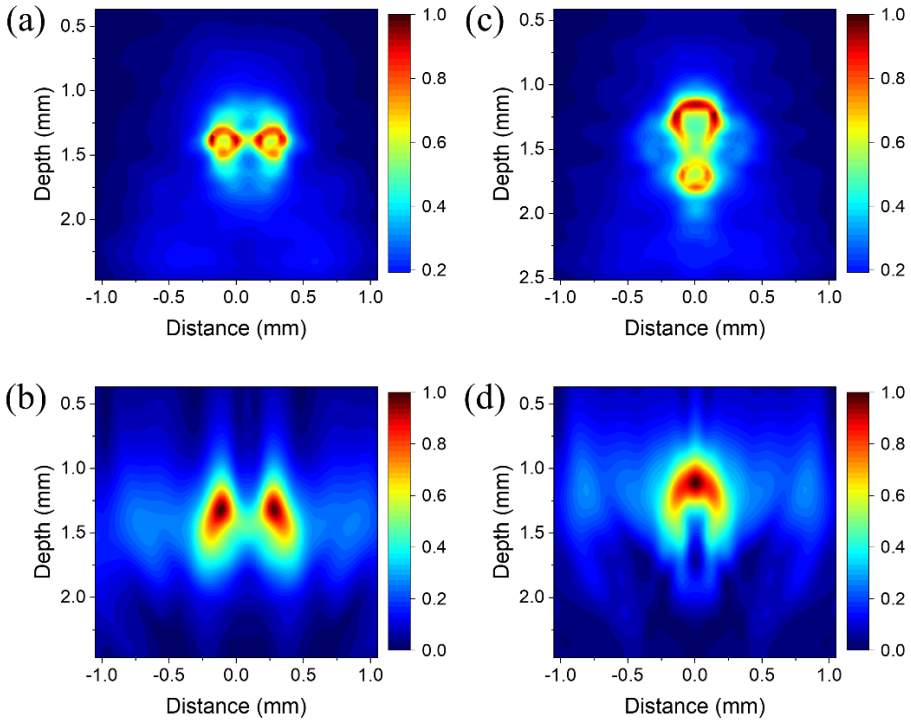

Fig. 5. (a) The LSM reconstruction of sample 2. (b) The corresponding DAS reconstruction using the direct longitudinal arrivals. (c) The LSM reconstruction of sample 3. (d) The corresponding DAS reconstruction using the direct longitudinal arrivals.

longitudinal wave. The image is again dominated by the direct reflection from the proximal surface of the upper hole while shadowing prevents direct rays from interacting with the bottom hole.

4. Experimental configuration

A scanning laser ultrasonic system is used to collect ultrasonic data across the sample surface. The excitation source is a Q-switched Nd:YAG laser ($\lambda = 1064$ nm) with a repetition rate of 15 Hz and a pulse width of 9 ns. The output is collimated and sent through a cylindrical lens to produce a line source with a FWHM of 50 µm and a length of 11 mm on the sample surface. The pulse energy is fixed at 0.85 mJ to operate in the thermoelastic regime. A motorized translation stage is used to scan the excitation laser over the surface. The resulting out-of-plane displacements are detected using a photorefractive crystal (PRC) based interferometer. The interferometer incorporates a CW frequency doubled Nd:YAG laser ($\lambda = 532$ nm) and a Bismuth Silicon Oxide photorefractive crystal. Addition details on the optical configuration and operation of the interferometer are available in the literature [28–31]. The output from the interferometer was captured on an oscilloscope with a 200 MHz bandwidth and transferred to a computer for processing.

Three aluminum alloy samples were used in this study. The defects in the samples were machined using precision electrical discharge machining (EDM). The hole diameters were measured using an optical microscope with the pixel size calibrated with a Ronchi ruling. The depth of the holes was 8 mm for sample 1 and 5 mm for samples 2 and 3. The sample geometries are consistent with those used in the simulation and shown in Fig. 1(b) with the caveat that for

Optics EXPRESS

sample 2 the average hole size (196 µm) was used in the simulations while in the EDM sample the left hole was found to be slightly smaller than the right hole (195 µm and 198 µm, respectively). The sample surfaces were polished to a mirror-like finish prior to inspection.

A LabView program was written to scan the translation stages to move both the sample and excitation position on the surface. The experiment involved fixing a single detection position by keeping the sample fixed and then moving the excitation position across the 121 locations within the imaging aperture. The detection location was then changed by moving the sample, and the excitation was once again scanned to illuminate the same 121 locations across the imaging aperture. The excitation line source was positioned parallel to the side drilled hole and the detection laser was 4.5 mm from the sample 1 edge and 2.5 mm from the edge for sample 2 and 3. The hole was positioned near the center of the 9.0 mm array aperture and at each source laser position, data was collected at all 121 receiver positions for full matrix acquisition. At each source and receiver distance, the waveform was averaged 100 times. To collect the background data set, the sample was translated such that the holes were outside of the field of view of the array. The background data in the defect free region requires only a small subset of the full matrix: at least one waveform at each source to receiver distance. Each background waveform was averaged 1000 times.

5. Results and discussion

We first compare the background data to the numerical simulation to ensure accurate modeling of the laser source and correct material properties. Note that as with the simulations, all waveforms are bandpass-filtered between 6 MHz - 21 MHz. Figure 6(a) shows a comparison of theory and experiment for a source-to-receiver distance of 1.95 mm. The waveforms show the arrival of the SSL, the SAW, and several direct and mode-converted reflections from the back surface (LL, SL, and SS). There is excellent agreement in both the shape of the waveform as well as times of the arrival. Waveforms were also compared at a source-to-receiver distance of 3.45 mm, where small differences in arrival times may be more evident. In Fig. 6(b), we magnify the time scale to examine later arrivals (after the SAW) and better compare bulk waves arrivals. The waveforms are again quite similar for both the mode-converted SL reflection from the back surface arriving at about 1.6 µs and the SS reflection from the back surface arriving at about 2.2 µs. Bulk wave arrivals that occur later in time in the simulation are close to the noise level in the experimental data.

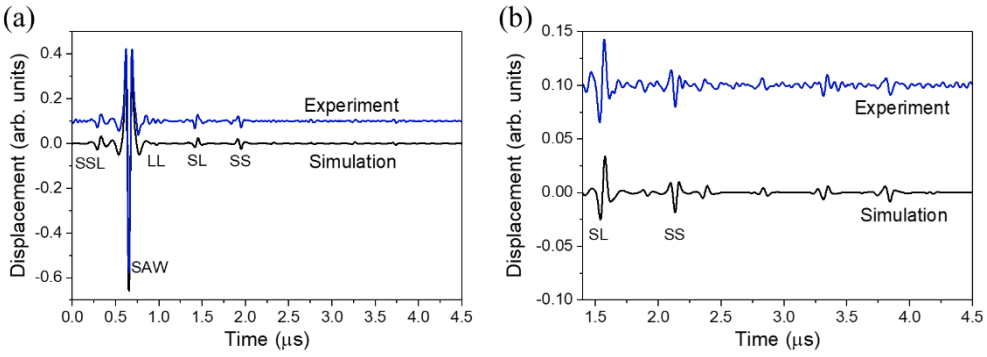

Fig. 6. Comparison of the experimental and simulated background data. (a) Waveforms when the source-to-receiver distance is 1.95 mm. (b) Arrival times and waveform shapes compared when zoomed in on the bulk arrivals from the back of the sample at a source to receiver distance of 3.45 mm.

Optics EXPRESS

Figure 7(a) shows a comparison of simulation and experimental waveforms for sample 1, at a source to receiver distance of 1.95 mm. The source was placed approximately 1.0 mm to the left of the hole, with the receiver to the right of the hole. As expected, we see arrival times consistent with the background data, including the SSL and SAW. We also see new features associated with scattering from the hole, including a direct shear wave reflection (SS) and a shear wave scattered from the hole and reflected from the back surface (SSS). Note that in the experiment the hole in sample 1 was slightly offset from the center of the aperture, and this geometry was mirrored in the simulation. The signal-to-noise ratio of the experimental defect data is lower than the background data due to the reduced number of averages. To isolate the scattered field, the background waveform is subtracted from the sample 1 waveform, and the results for both the simulation and experiment are shown in Fig. 7(b). In the scattered field for the experimental data, there are some residual surface acoustic wave arrivals. We believe that this is due to sight changes in the surface condition across the sample affecting the laser source. The issue is exacerbated by the fact that SAW signal has a large amplitude relative to the signal from the scattered field. Just after the SAW residual, there is reasonable agreement between simulation and experiment in the arrivals of the SL, SS, and SSS reflections from the hole. At this source and receiver location, however, additional arrivals are near the noise level and difficult to identify. Figure 7(c) shows the scattered signals from all 121 detector positions across the array, with the color bar indicating the displacement and the x-axis indicating the detector location. Here we observe the wavefronts associated with several of the arrivals. In addition, we observe the residual SAW signal from the direct field and an edge artifact associated with the line source interacting with the sample edge.

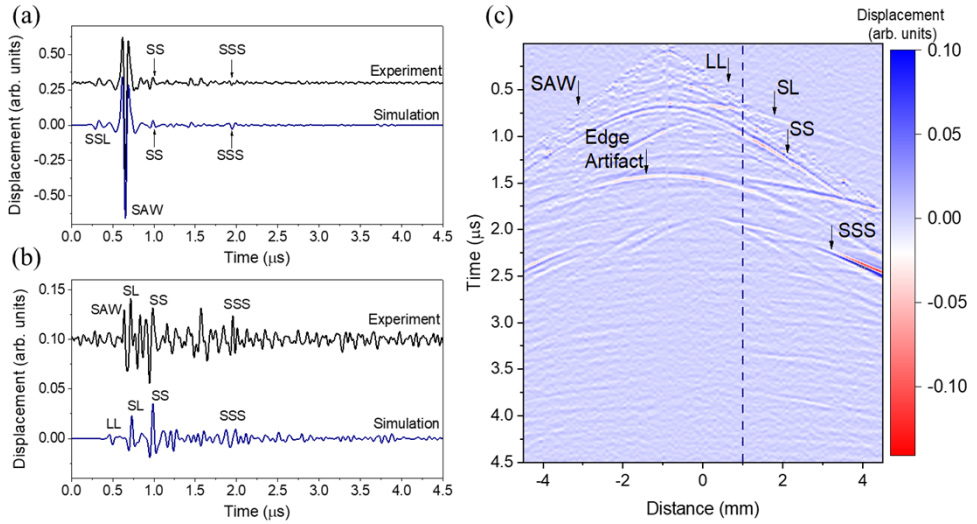

Fig. 7. (a) Comparison of experimental and simulated waveforms in sample 1 when the source and receiver are 1.95 mm apart. (b) Comparison of the experimental and simulated scattered signals. (c) A waterfall plot of the experimental waveforms at all the detector locations within the aperture. The dashed line is the location of the waveform in (b).

Figure 8(a) shows the LSM reconstruction from the experimental scattered field data for sample 1. The inset in the figure shows an image of the hole taken using an optical microscope. The LSM image captures most of the hole boundaries, with some distortion and a relatively weak bottom surface. To compare the result to simulation, 0.5% random noise is added to the simulation data set, with noise again defined by the standard deviation as a percentage of SAW amplitude in the reconstruction bandwidth Ω. The result is shown in Fig. 8(b). The image contrast with the background is sharper in the simulation results, which we believe is primarily due to the

Optics EXPRESS

incomplete subtraction of the background signal in the simulated data. The remaining SAW residual and edge artifact effectively add additional noise to the experimental data. For a more quantitative measure of the visibility of the hole, we take the difference between the maximum and minimum intensity of the image and divide this by the standard deviation of the background, defined as the region outside a 500×500 µm square centered on the hole. This gives a value of 19.2 for the simulated image and 13.1 for the experimental image. By simply taking the distance between the peak amplitude values across the center of the hole, the hole size is estimated to be very close to 270 µm.

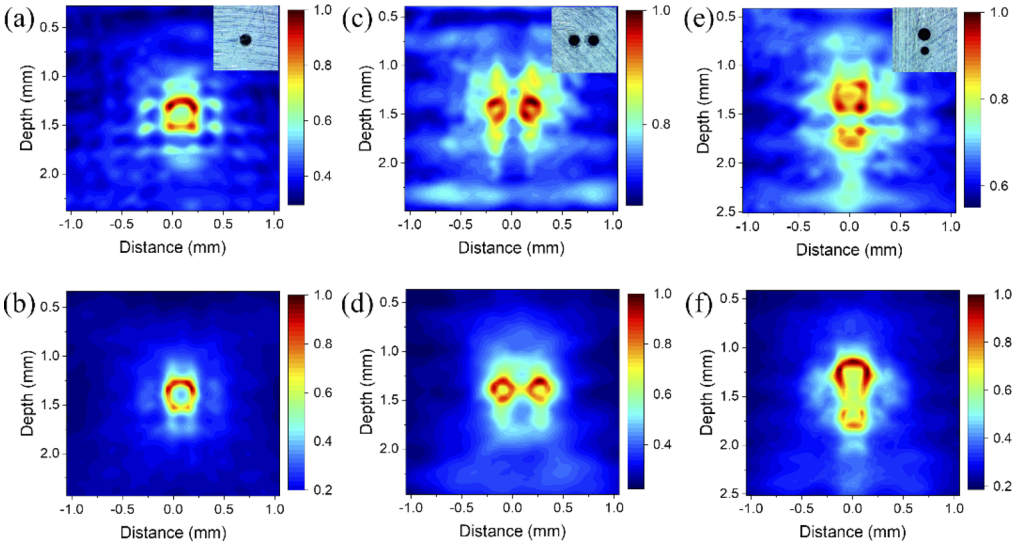

Fig. 8. (a), (c), (e) LSM reconstruction of experimental data of the three sample in the 6 MHz-21 MHz frequency range. (b), (d), (f) The corresponding LSM reconstruction of the simulation data with a similar amount of noise added. The insets in the top row are microscope images of the samples.

The experimental and simulation results for sample 2 are given in Figs. 8(c) and 8(d), respectively. While the experimental results clearly show the presence of two defects, the image is blurred, and contrast is reduced compared to the simulation. Sample 3 LSM images for experiment and simulation are given in Figs. 8(e) and 8(f), respectively. The experimental results are again blurred in comparison with simulation data and additional artifacts are present. Nevertheless, imaging a smaller feature with direct rays blocked by the larger hole is challenging and the LSM algorithm is effective in isolating some of the hole boundaries and indicating the presence of two features. For comparison, the DAS image reconstructions for sample 2 using direct longitudinal and shear waves are given in Figs. 9(a) and 9(b), respectively, while those for sample 3 are shown in Figs. 9(c) and 9(d), respectively. One advantage of DAS is that the image contrast is much higher than LSM, and thus DAS is effective in detecting the presence of a scatterer within the field of view. However, in the absence of further post processing to combine multiple ray paths (such as half-skip or full-skip modes in the case of sample 3, for example) shape reconstruction is not possible. This is a key advantage of using model-based imaging approaches such as LSM for laser ultrasonic signals.

We used a 15 Hz experimental repetition rate laser, and thus we restricted the signal averaging to 100x for the collection of a 121×121 full matrix of data. Higher repetition rate lasers (up to 10 kHz and above) are commonly available and could lead to significant improvements in signal-to-noise ratio and LSM reconstruction. Effective subtraction of the background data

Optics EXPRESS

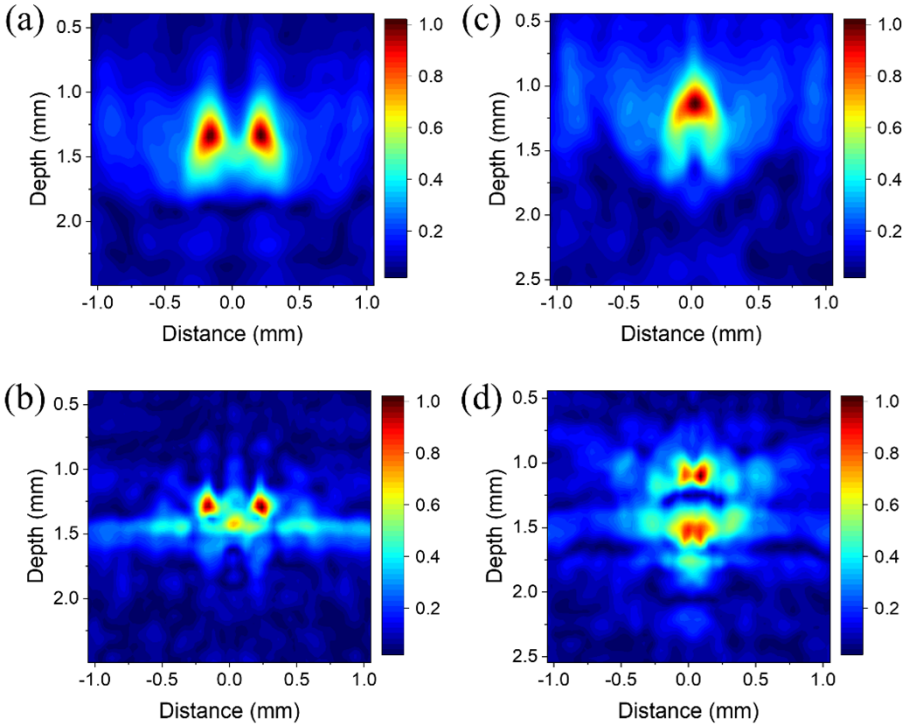

Fig. 9. DAS reconstruction of experimental data for the 2-hole objects in the 6 MHz-21 MHz frequency range. Sample 2 is reconstructed using the (a) direct longitudinal arrivals and (b) direct shear arrivals. Sample 3 is reconstructed using the (c) direct longitudinal arrivals and (d) direct shear arrivals.

remains challenging, and for laser ultrasonic measurements this requires uniformity of the sample surface as well as stability of the laser source. While this may limit some industrial applications, we believe that improvement in subtracting the background over what we have shown here is possible through careful surface preparation and, in this case, by taking the reference data near an edge to remove the edge artifact. Given the excellent agreement between background simulation and experiment, it may also be possible to use a simulated data set for background subtraction.

6. Conclusion

We demonstrate the usefulness of the linear sampling method (LSM) from inverse scattering theory for imaging with laser ultrasonic data. Using experiments and finite element time domain simulations, we showed that the LSM, in the presence of low background noise, can perform accurate shape reconstruction of single and multiple side-drilled holes, and produce images with high resolution and well-defined boundaries. This approach has the advantage over DAS in that it uses all of the ultrasound ray paths to reconstruct scatterers within the field of view. LSM can therefore complement DAS, providing an attractive alternative when accurate reconstruction of subsurface features is required.

Funding. Lawrence Livermore National Laboratory (DE-AC52-07NA27344).

Acknowledgments. This work was performed under the auspices of the U.S. Department of Energy by Lawrence Livermore National Laboratory under Contract DE-AC52-07NA27344 and was supported by the LLNL-LDRD Program under Project No. 20-SI-001. The LLNL document release number is LLNL-JRNL-841201.

Disclosures. The authors declare no conflicts of interest.

Optics EXPRESS

Data availability. Data underlying the results presented in this paper are not publicly available at this time but may be obtained from the authors upon reasonable request.

References

1. S. J. Davies, C. Edwards, G. S. Taylor, and S. B. Palmer, "Laser-generated ultrasound: its properties, mechanisms and multifarious applications," J. Phys. D: Appl. Phys. **26**(3), 329–348 (1993).
2. C. M. Hernandez, T. W. Murray, and S. Krishnaswamy, "Photoacoustic characterization of the mechanical properties of thin films," Appl. Phys. Lett. **80**(4), 691–693 (2002).
3. F. Zhang, S. Krishnaswamy, and C. M. Lilley, "Bulk-wave and guided-wave photoacoustic evaluation of the mechanical properties of aluminum/silicon nitride double-layer thin films," Ultrasonics **45**(1-4), 66–76 (2006).
4. R. Quintero, F. Simonetti, P. Howard, J. Friedl, and A. Sellinger, "Noncontact laser ultrasonic inspection of Ceramic Matrix Composites (CMCs)," NDT&E Int. **88**, 8–16 (2017).
5. M. Maalekian, R. Radis, M. Militzer, A. Moreau, and W. J. Poole, "In situ measurement and modelling of austenite grain growth in a Ti/Nb microalloyed steel," Acta Mater. **60**(3), 1015–1026 (2012).
6. J. Zhang, J. Wu, X. Zhao, S. Yuan, G. Ma, J. Li, T. Dai, H. Chen, B. Yang, and H. Ding, "Laser ultrasonic imaging for defect detection on metal additive manufacturing components with rough surfaces," Appl. Opt. **59**(33), 10380 (2020).
7. G. Davis, R. Nagarajah, S. Palanisamy, R. A. R. Rashid, P. Rajagopal, and K. Balasubramaniam, "Laser ultrasonic inspection of additive manufactured components," Int J Adv Manuf Technol **102**(5-8), 2571–2579 (2019).
8. Y. Zhan, C. Liu, J. Zhang, G. Mo, and C. Liu, "Measurement of residual stress in laser additive manufacturing TC4 titanium alloy with the laser ultrasonic technique," Mater. Sci. Eng., A **762**, 138093 (2019).
9. A. Blouin, D. Levesque, C. Neron, D. Drolet, and J.-P. Monchalin, "Improved resolution and signal-to-noise ratio in laser-ultrasonics by SAFT processing," Opt. Express **2**(13), 531 (1998).
10. D. Lévesque, A. Blouin, C. Néron, and J.-P. Monchalin, "Performance of laser-ultrasonic F-SAFT imaging," Ultrasonics **40**(10), 1057–1063 (2002).
11. J. Zhang, B. W. Drinkwater, P. D. Wilcox, and A. J. Hunter, "Defect detection using ultrasonic arrays: The multi-mode total focusing method," NDT&E Int. **43**(2), 123–133 (2010).
12. K. Sy, P. Bredif, E. Iakovleva, O. Roy, and D. Lesselier, "Development of methods for the analysis of multi-mode TFM images," J. Phys.: Conf. Ser. **1017**(1), 012005 (2018).
13. N. Portzgen, D. Gisolf, and D. Verschuur, "Wave equation-based imaging of mode converted waves in ultrasonic NDI, with suppressed leakage from nonmode converted waves," IEEE Trans. Ultrason., Ferroelect., Freq. Contr. **55**(8), 1768–1780 (2008).
14. R. L. T. Bevan, N. Budyn, J. Zhang, A. J. Croxford, S. Kitazawa, and P. D. Wilcox, "Data Fusion of Multiview Ultrasonic Imaging for Characterization of Large Defects," IEEE Trans. Ultrason., Ferroelect., Freq. Contr. **67**(11), 2387–2401 (2020).
15. N. Budyn, A. J. Croxford, R. L. T. Bevan, J. Zhang, and P. D. Wilcox, "Characterisation of small embedded two-dimensional defects using multi-view Total Focusing Method imaging algorithm," NDT&E Int. **119**, 102413 (2021).
16. P. D. Wilcox, A. J. Croxford, N. Budyn, R. L. T. Bevan, J. Zhang, A. Kashubin, and P. Cawley, "Fusion of multi-view ultrasonic data for increased detection performance in non-destructive evaluation," Proc. R. Soc. A. **476**(2243), 20200086 (2020).
17. M. Fink, "Time reversal of ultrasonic fields. I. Basic principles," IEEE Trans. Ultrason., Ferroelect., Freq. Contr. **39**(5), 555–566 (1992).
18. B. E. Anderson, M. Griffa, T. J. Ulrich, and P. A. Johnson, "Time reversal reconstruction of finite sized sources in elastic media," J. Acoust. Soc. Am. **130**(4), EL219–EL225 (2011).
19. A. J. Devaney, E. A. Marengo, and F. K. Gruber, "Time-reversal-based imaging and inverse scattering of multiply scattering point targets," J. Acoust. Soc. Am. **118**(5), 3129–3138 (2005).
20. D. Colton and A. Kirsch, "A simple method for solving inverse scattering problems in the resonance region," Inverse Problems **12**(4), 383–393 (1996).
21. F. Cakoni, D. Colton, and H. Haddar, *Inverse Scattering Theory and Transmission Eigenvalues* (Society for Industrial and Applied Mathematics, 2016).
22. Y. Guo, P. Monk, and D. Colton, "The linear sampling method for sparse small aperture data," Applicable Analysis **95**(8), 1599–1615 (2016).
23. A. C. Prunty, R. K. Snieder, and C. Sens-Schönfelder, "Acoustic imaging using unknown random sources," J. Acoust. Soc. Am. **149**(1), 499–507 (2021).
24. F. Pourahmadian and H. Yue, "Laboratory application of sampling approaches to inverse scattering," Inverse Problems **37**(5), 055012 (2021).
25. V. Baronian, L. Bourgeois, B. Chapuis, and A. Recoquillay, "Linear sampling method applied to non destructive testing of an elastic waveguide: theory, numerics and experiments," Inverse Problems **34**(7), 075006 (2018).
26. C. Holmes, B. W. Drinkwater, and P. D. Wilcox, "Post-processing of the full matrix of ultrasonic transmit–receive array data for non-destructive evaluation," NDT&E Int. **38**(8), 701–711 (2005).
27. Rainer, Kress, V, Maz'ya, and V Kozlov, *Linear Integral Equations* (Springer, 1989), 82.
28. R. K. Ing and J-P Monchalin, "Broadband optical detection of ultrasound by two-wave mixing in a photorefractive crystal," Appl. Phys. Lett. **59**(25), 3233–3235 (1991).

Optics EXPRESS

29. A. Blouin and J. Monchalin, "Detection of ultrasonic motion of a scattering surface by two-wave mixing in a photorefractive GaAs crystal," Appl. Phys. Lett. **65**(8), 932–934 (1994).
30. T. W. Murray, "Multiplexed interferometer for ultrasonic imaging applications," Opt. Eng **40**(7), 1321 (2001).
31. T. W. Murray, H. Tuovinen, and S. Krishnaswamy, "Adaptive optical array receivers for detection of surface acoustic waves," Appl. Opt. **39**(19), 3276 (2000).